Journal of Advanced Research 28 (2021) 165–174

Contents lists available at ScienceDirect

Journal of Advanced Research

journal homepage: www.elsevier.com/locate/jare

Development of photosensitizer-loaded lipid droplets for photothermal therapy based on thiophene analogs

Yue Xu [a,1], Hua Li [a,1], Lixue Fan [a], Yisha Chen [a], Li Li [a], Xiaojing Zhou [b], Ruixi Li [a], Yuru Cheng [c], Haiyan Chen [a,*], Zhenwei Yuan [a,*]

[a] Department of Biomedical Engineering, School of Engineering, China Pharmaceutical University, 24 Tongjia Lane, Gulou District, Nanjing 210009, China
[b] Georgetown University, 3700 O St NW, Washington, DC 20057, USA
[c] School of Pharmacy, Jiangxi University of Traditional Chinese Medicine, 818 Xingwan Road, Wanli District, Nanchang City, Jiangxi Province, China

GRAPHICAL ABSTRACT

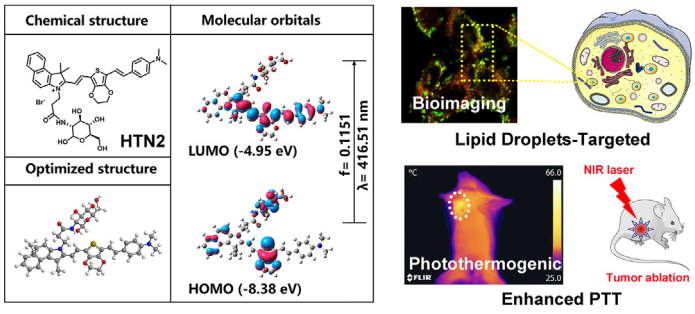

ARTICLE INFO

Article history:
Received 4 June 2020
Revised 1 August 2020
Accepted 3 August 2020
Available online 06 August 2020

Keywords:
Photothermal therapy
Thiophene analog
D-π-A structure
Lipid droplets
Tumor ablation

ABSTRACT

Photothermal therapy (PTT) was considered as one of the most promising cancer therapies to overcome the severe side effects caused by chemotherapy. Hence, four thiophene analogs were developed to construct novel organic photothermal agents (PTAs) for many biomedical applications in cancer biosensing and photothermal therapies. The efficacy of four compounds was demonstrated by studies of photothermal properties as well as photothermal therapeutic effects. Besides, tumor ablation experiments indicated that HTN2 can effectively suppress tumors in vivo and in vitro as a novel PTA. Hence, PTAs that we designed and synthesized with their advantage of good biocompatibility and facile structural design could be candidates for PTT.

Introduction

Photothermal therapy (PTT) was considered as one of the most promising cancer therapy to overcome the severe side effects caused by chemotherapy [1,2]. The photothermal responses can be exploited for many biomedical applications in cancer biosensing and photothermal therapies. Designing smarter biotherapeutic agents is one of the most challenging goals in current biomaterials science [3]. Inorganic nanomaterials, namely, gold nanoparticles

Peer review under responsibility of Cairo University.
* Corresponding authors.
E-mail addresses: chenhaiyan@cpu.edu.cn (H. Chen), yuanzhenwei@cpu.edu.cn (Z. Yuan).
[1] These authors contributed equally to this work.

https://doi.org/10.1016/j.jare.2020.08.003
2090-1232/

[4,5], copper sulfide nanoparticles [6–8], carbon nanoparticles [9–12] and so on [13–17], are commonly used as photothermal materials. However, some potential limitations, such as poor biodegradability and potential toxicity, limit their biological applicability [18]. Hence, with their advantage of good biocompatibility and facile structural design, small molecular organic PTAs could be candidates for PTT.

Recently, some suitable NIR organic dyes, such as cyanine (Cy) dyes [19–21], phthalocyanine [22,23], and BODIPY [24–26], have been developed as PTAs. Inspired by previous studies, substantial effort has been devoted to developing more effective organic PTAs. To achieve superior optical absorption properties, we found that a certain amount of PTT agent with a D-π-A structure (electron donor-π- conjugated bridge-electron acceptor) was essential, and greater extents of conjugation resulted in lower fluorescence quantum yields. Thiophenes are widely recognized as sensitizers in D-π-A compounds due to their tunable spectroscopic properties and polarizability. When present in a D-π-A system, thiophenes enhance both the extent of conjugation and stability [27]. Currently, many successful polymers with thiophene as their basic unit have been designed for thermoelectric devices. Through a click reaction, a series of thiophene derivatives and 7,7,8,8-tetracyano quiodimethane (TCNO) conjugates have been used for a combination of PTT and PA imaging [28]. Therefore, using thiophene analogs to construct organic PTAs has great potential.

LDs play an important role in cellular lipid homeostasis and energy metabolism. Many studies have shown that the number and size of LDs are related to the cellular metabolic state. Recent studies have shown that they also play an important role in many aspects of cancer development [29–31]. Highly proliferating cancer cells exhibit strong lipid affinities through the overactivation of endogenous synthesis and increasing the uptake of exogenous lipids and lipoproteins. Studies on the abundance of LDs in different kinds of breast cancer cell lines have shown a direct correlation between the LDs and the cell lines' degree of malignancy [32]. Moreover, cancer cells exhibit higher LDs content than normal cells because cancer cells sustain their proliferation by increasing lipogenesis [33]. This result in the accumulation of cholesteryl esters (CEs) in LDs, which greatly increased the proliferation of cancer, improves the invasive ability of cancer and promoted tumor growth. Excessive lipids and cholesterol in cancer cells are stored in LDs. Thus, high levels of LDs and CEs in tumors are considered biomarkers of cancer aggressiveness. In summary, inhibition of tumor growth and metastasis spread could be achieved by blocking utilization or breaking down LDs.

To achieve a truly synergistic and even enhanced PTT and LD-targeting effects, a suitable PTA should be selected. In this study, four thiophene analogs were designed and synthesized, and LD-targeting PTAs may be the main cause of tumor ablation and inhibition after irradiation. The designed compounds had three components:an electron-withdrawing group, a bridging groups and an electron-donating group. This work provides a new convenient design strategy for targeting LDs by using thiophene analogs to enhance the PTT effect on tumors.

Results and discussion

Synthesis and characterization

HTN1-4, organic molecules with near-infrared fluorescence, were designed with an electron-withdrawing group (1,1,2-trimethylbenz[e]indole salt), a bridging group (thiophene or 3,4-ethylenedioxythiophene) and an electron-donating group (4-ethenyl-N,N-dimethylaniline) and synthesized via condensation and coupling reactions. The newly formed double bond allowed conjugation between the double bonds in the thiophene and benzene rings, causing a redshift in the maximum absorption wavelength by increasing the degree of conjugation. We installed water-soluble D-glucosamine hydrochloride on compounds **HTN2** and HTN4 to increase their water solubility.

To understand the charge transfer in HTN1-4, we used TD-DFT with B3LYP functional analysis at the 6-31G* level of theory to calculate the energies of the highest occupied molecular orbital (HOMO) and the lowest unoccupied molecular orbital (LUMO) of HTN1-4. The HOMO and LUMO electron clouds of HTN1-4 are all located in the π-conjugated regions (thiophene ring and 4-ethenyl-N, N-dimethylaniline ring) except for the benzindole ring, which shows no obvious intramolecular charge transfer (ICT) process. The results of the DFT analysis of HTN2 are shown in Fig. 1b and the main electron excitations of HTN1-4 are shown in Fig. S3.

Spectral and photothermal properties

As shown in Fig. 2a, **HTN2** had a wider absorption band in the NIR region than other PTAs. To explore the photostability of photosensitizers in different pH environments, solutions of different pH values were configured to simulate a complex physiological environment. The stability was demonstrated by monitoring the UV absorption of the **HTN1-4** and finding no significant wavelength migration (Fig. 2b and S4). The absorption spectra of HTN3 and HTN4 extended from 450 nm to 900 nm, while those of HTN1 and HTN2 extended from 500 to 1000 nm. The fluorescence maxima of HTN1-4 were all at approximately 820 nm (Fig. S5). Theoretically, electrons in many compounds will rapidly transition to the lowest excited singlet state (S1) after photoexcitation and then return to the ground state by emitting photons (fluorescence) or nonradiative relaxation [34]. **HTN2** had the weakest relative fluorescence intensity of the four PTAs under the same test conditions (Fig. S5). The photothermal effect of **HTN2** likely mainly occurs through a nonradiative relaxation process because it has the strongest absorption and the weakest fluorescence intensity, which would give it the best PCE.

To better validate this hypothesis, we designed and synthesized the control compound HTN without thiophene units. The fundamental optical properties of HTN1-4 were conducted, including maximum absorption/emission wavelength in different solvents, the molar extinction coefficients (Fig. S6–S8). The related results showed that HTN2 exhibits some solvent effect and has the potential to localize in LDs according to our previous research. As we reported previously [35], thiophene analogs may have the ability to target lipid droplets (LDs). The critical role played by the thiophene unit was investigated by comparing the fluorescence signals and the photothermal effect between control compound HTN and HTN1-4. Fluorescence intensity of HTN is much higher than other compounds in the same solvent conditions (Fig. S9). Meanwhile, the HTN also shows almost no photothermal effect as expected (Fig. S10). These results demonstrated that thiophene units play an important role in the photothermal effect.

To further elucidate the relative photothermal capabilities of the four PTAs and validate our hypothesis, their conversion efficiencies under 808-nm laser irradiation were compared, and DMSO was used as the solvent to guarantee complete dissolution of the four PTAs. Different concentrations of HTN1-4 (0 mM, 0.25 mM, 0.5 mM and 1 mM) were exposed to 808-nm and 635-nm laser irradiation at different power densities (0, 0.4, 0.8, and 1.2 W/cm^2) for 600 s. As shown in Fig. S11, the temperature change was well correlated with the laser power and concentration. **HTN2** showed effective thermal conversion capacity, as the temperature of **HTN2** solutions at different concentrations (0.25 mM, 0.5 mM, and 1 mM) increased by 30.2 °C to 47.4 °C under a laser power density of 0.8 W/cm^2 (Fig. 2**c**). To evaluate the photothermal

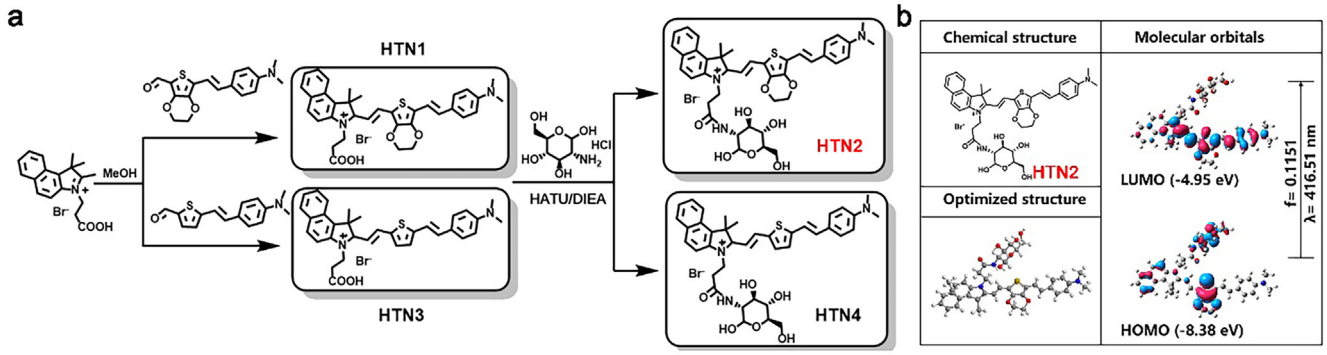

Fig. 1. Schematic of **HTN1-4** synthesis and DFT calculate of **HTN2**.

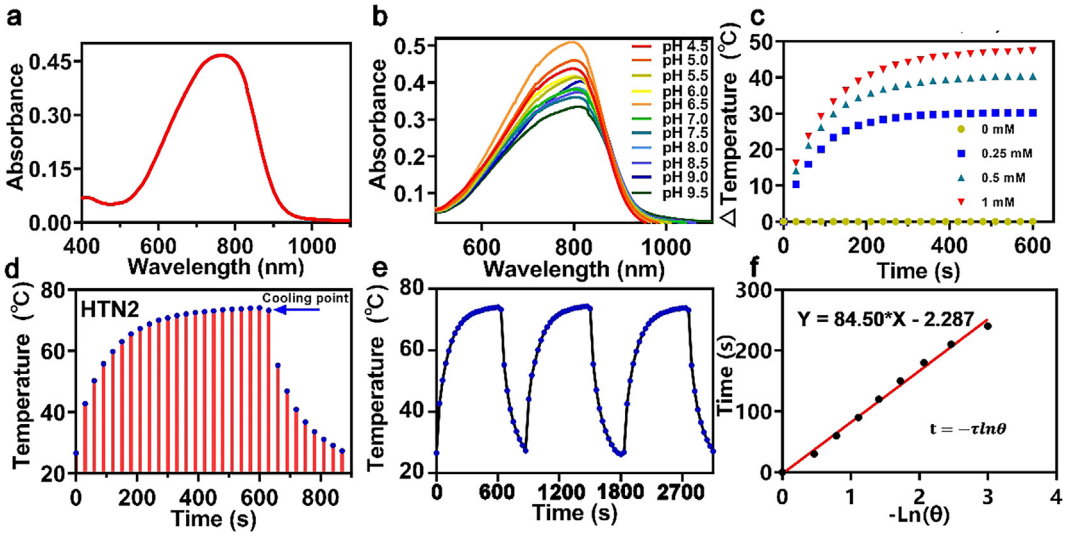

Fig. 2. Ultraviolet absorption spectrum of **HTN2** (a) in PBS/DMSO solution (99/1, 0.10 M, pH 7.4) at 37 °C (b) and at different pH values (4.5, 5.0, 5.5, 6.0, 6.5, 7.0, 7.5, 8.0, 8.5, 9.0, and 9.5). (c) Constant irradiation at 0.8 W/cm^2 with varying **HTN2** concentrations (0, 0.25, 0.50, and 1.0 mM, 808 nm). (d) Photothermal effects observed upon irradiating **HTN2** with 808-nm laser light (0.8 W/cm^2) for 600 s and then stopping the irradiation and continuing to record the temperature. (e) **HTN2** (1 mM) over several ON/OFF cycles involving irradiation with an 808 nm laser (0.8 W/cm^2) and cooling and repeat the process three times. (f) The plot of Ln(θ) of **HTN2** as a function of time, the value of θ is detailed in the formula of the experimental method.

properties of **HTN2** in more detail, we measured the PCE (η) according to a reported method [36,37]. First, we increased the temperature of the **HTN2** solution (1 mM) to a steady-state under 808-nm laser irradiation (0.8 W/cm^2). Immediately after stopping the laser irradiation, the temperature drop was recorded to calculate the rate of heat transfer from the **HTN2** solution to the environment (Fig. 2d). According to Fig. 2e and the formula in S13, the PCE (η) of **HTN2** was approximately 27.18%, which is higher than those of the other PTAs. According to the same calculation method, η of HTN1, 3 and 4 were 23.2%, 18.5%, and 22.1%, respectively. The excellent PCE of **HTN2** was consistent with its weak fluorescence intensity, further confirming that the photothermal effect of **HTN2** mainly occurs through a nonradiative relaxation process and converts NIR light into heat. Because of both its PCE and water solubility, **HTN2** has greater potential as a PTA than the other three PTAs.

Cell affinity detection

We observed the relationship between **HTN2** and cell incubation time by two-dimensional monolayer cell culture and showed a good linear relationship by fluorescence semi-quantitative analysis that the cell intake increased with time (Fig. 3a–b). Two-dimensional monolayer cell cultures are often used to evaluate the effects of small molecules; however, this simple model lacks some intercellular effects and interactions with the matrix. Therefore, this model cannot fully simulate the complex biochemical environment in the body. We used a three-dimensional in vitro tumor sphere model to predict the behavior of **HTN2**, and this model is often used in physiological experiments. The three-dimensional model of the tumor sphere was constructed using 2% low-melting agarose to simulate the hypoxia and low nutrient supply characteristic of tumor cells, resulting in a microenvironment similar to tumor cells. The physiological characteristics of this model are also similar to avascular tumor nodules, micro metastases, and intravascular solid tumors. Therefore, we chose this three-dimensional tumor model to test the ability of **HTN2** to penetrate the tumor microenvironment. The process for constructing the three-dimensional tumor sphere is shown in Fig. 3c. After incubation with **HTN2** for two hours, the tumor penetration ability of **HTN2** was observed by LSCM. As shown in Fig. 3d–e, **HTN2** had good penetration and the significant fluorescence signal can be observed in the range from 25 μm to 40 μm in the middle of the tumor sphere. The results also revealed that it may have good bioimaging potential. Based on the above experiments, we assumed that **HTN2** can effectively

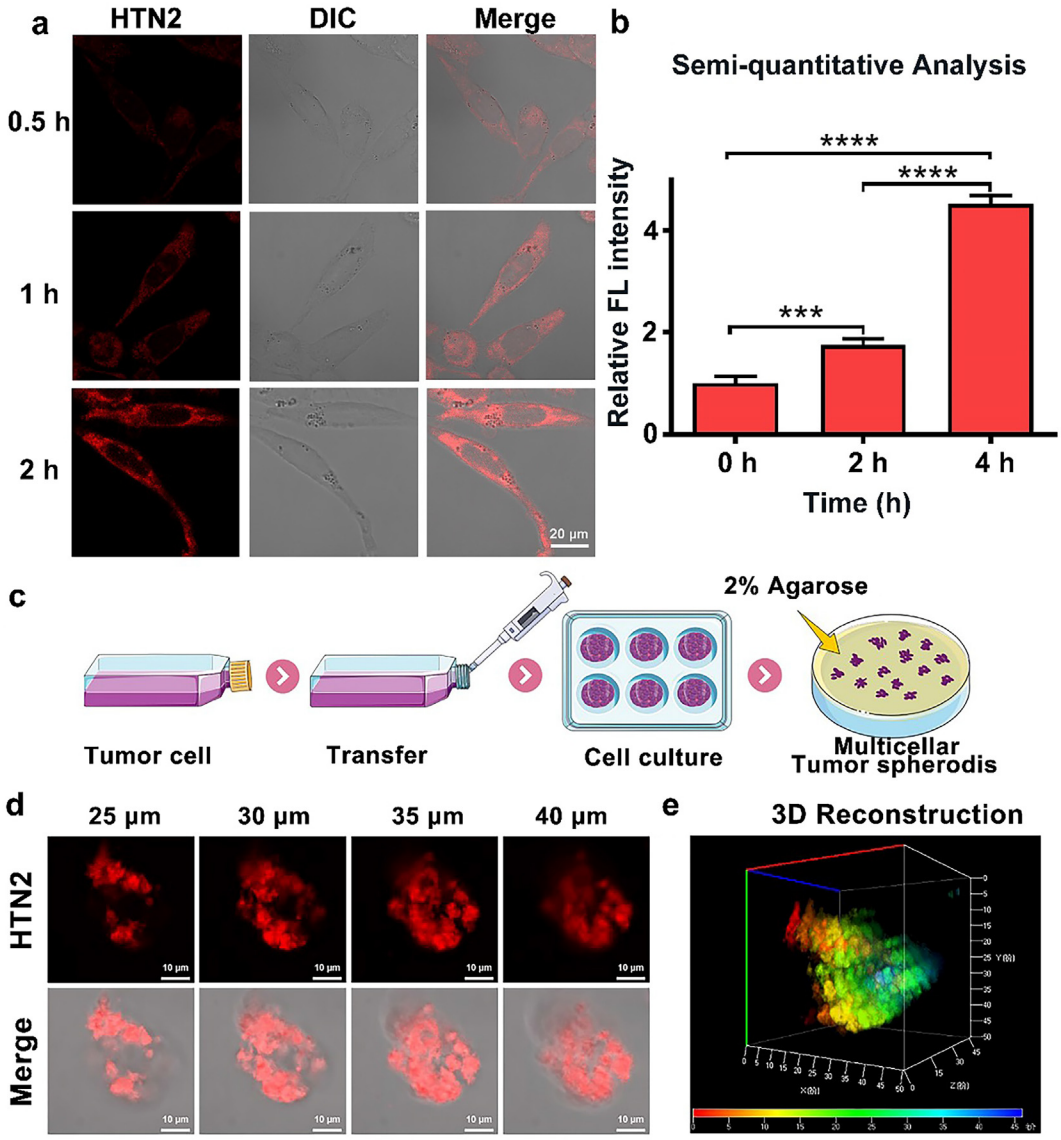

Fig. 3. (a) U87 cells treated with **HTN2** (20 μM, λ_{ex} = 647 nm) for 0.5 h, 1 h and 2 h. (b) Semi-quantitative analysis of relative fluorescence intensity with the change over time. (c) Schematic of the construction of the three-dimensional tumor sphere model. (d) Overlay images (5 μm) were acquired from the top surface to the equatorial plane (0–60 μm) of the tumor sphere by LSCM, middle section of the image and the Z-stack map of the tumor sphere (25–40 μm) was analyzed. (e) 3D reconstruction from the fluorescence images.

penetrate tumors and has good potential for biological applications.

Subcellular localization and photothermal effects in vitro

In order to ensure that structurally modified compound still have this property, the subcellular localization of **HTN2** was determined by co-staining with an organelle positioning probe (Fig. 4a). Droplit™ Red-stained cells eventually showed excellent overlap with **HTN2**. Linear profile analysis showed a strong correlation between **HTN2** and Droplit™ Red (Fig. 4b). The Pearson's overlap coefficient between **HTN2** and LDs was 0.80, which indicates significant correlation between **HTN2** and Droplit™ Red (Fig. 4c). All results indicated that **HTN2** is subcellularly localized to the LDs. Numerous papers [38] have reported that deregulation of lipid metabolism is an important metabolic marker in tumor cells. Hence, destroying LDs by the photothermal effect to inhibit over proliferation of tumor cells may be a promising therapeutic strategy for human cancer. Generally, higher intensity lasers offer deeper penetration. However, proper laser power can achieve a better PTT effect and avoid damaging normal tissue. Studies [39] have shown that photothermal radiation can cause cell death through necrosis or apoptosis depending on the intensity of the radiation. However, necrosis may affect the treatment outcome by triggering a proinflammatory response, which could promote tumor growth. In contrast, the cell membrane can be completely retained during apoptosis. Due to the integrity of the cell membrane, dying cells can be recognized and taken up by phagocytic cells over time, reducing unwanted inflammatory responses and improving therapeutic performance [40]. Thus, determining the appropriate laser power is important for achieving effective treatment. Cells stained with **HTN2** and PI were imaged by laser confocal microscopy to observe any PTT-induced morphological changes in the cells and the survival ratios at different laser powers. The control group was not subjected to laser irradiation, and the photothermal treatment groups were irradiated at different intensities (0.4 W/cm^2

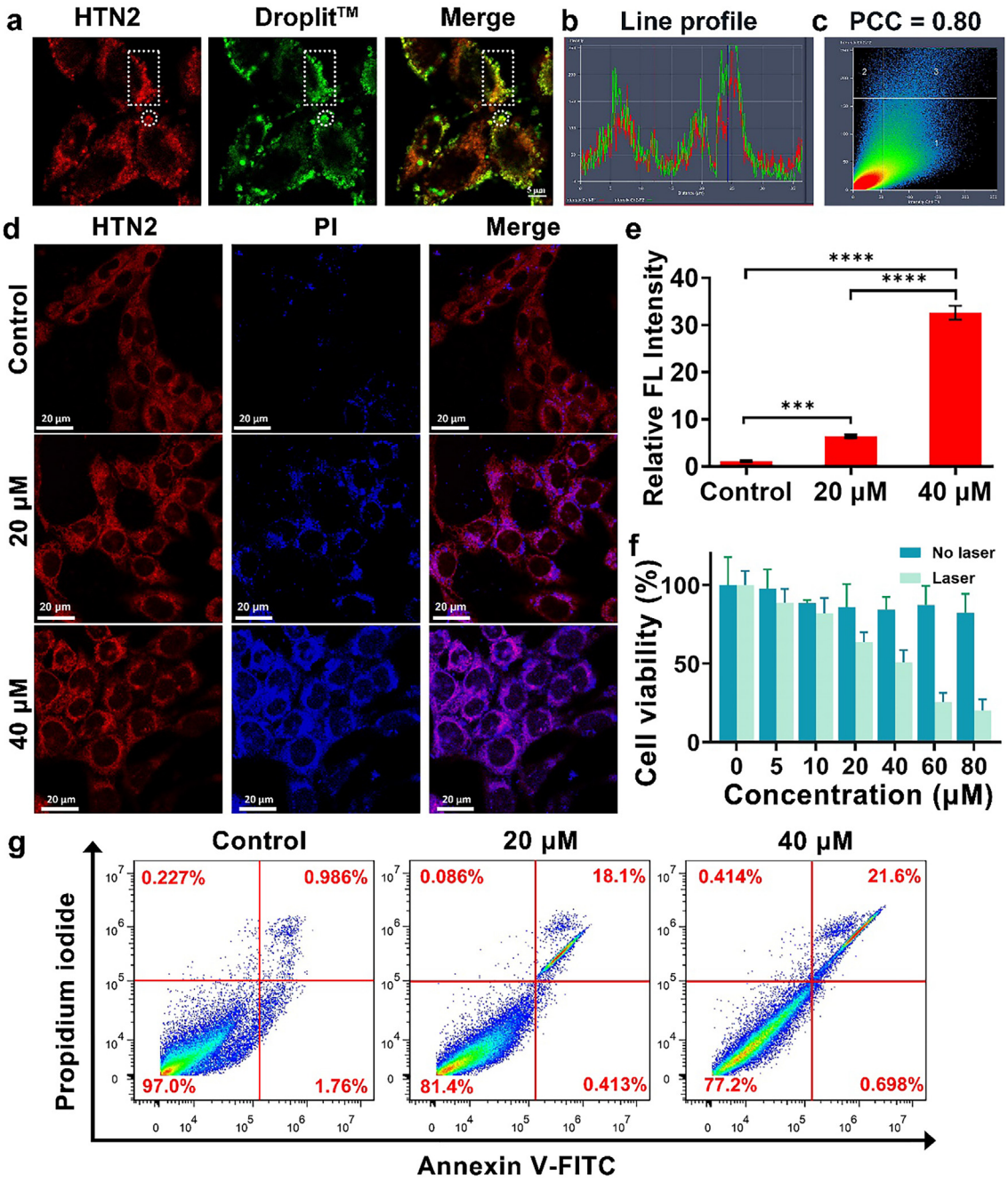

Fig. 4. Confocal laser scanning microscopy images (a) U87 cells treated with **HTN2** (20 μM, λ_{ex} = 647 nm) for 0.5 h then stained with the LDs commercial probe (10 μM, λ_{ex} = 555 nm) for 2 h. Overlaid images of **HTN2** and Droplit™ Red staining. Scale bars: 5 μm, PBS buffer. (b) Line profile and (c) Pearson's colocalization coefficient of **HTN2** in U87 cells compared with the commercial LD probe. (d) The confocal fluorescence images of U87 cells incubated for 2 h with 20 μM **HTN2** and 5 μM PI (DEAD Cell Imaging Kit) under different 808-nm laser powers (0 W/cm^2, 0.4 W/cm^2 and 0.8 W/cm^2). (e) Semiquantitative analysis of the relative fluorescence intensity of each group by a DEAD Cell Imaging Kit. (f) Cell viability of U87 cells incubated with different concentrations of **HTN2** for 12 h compared to viability in the group subjected to photothermal therapy by an 808-nm laser (0.8 W/cm^2). (g) Flow cytometry analysis of Annexin V-FITC/propidium iodide-stained U87 cells with saline and **HTN2** (20 μM and 40 μM) incubation after exposure to an 808-nm laser (0.8 W/cm^2).

and 0.8 W/cm^2). As illustrated in Fig. 4d, **HTN2** can be used as a superb near-infrared dye for fluorescence imaging of cells to observe cell morphology. Due to the advantages of bioimaging, significant cell atrophy could be observed in U87 cells in the photothermal treatment groups. The U87 cells were also stained with a DEAD Cell Imaging Kit, and the relative fluorescence intensity of PI in another channel showed that the degree of apoptosis was positively correlated with concentration (Fig. 4e). Subsequently, to determine the suitability of **HTN2**, U87 cells treated with a safe dose of **HTN2** were studied by a standard MTT assay to calculate cell viability, and the results are shown in Fig. 4f, and the of the cytotoxicity assays of **HTN2** are show for comparison. As expected, the average cell viability of U87 exceeded 85% after 2 h of incubation with different concentrations of **HTN2**, indicating that **HTN2** has low cytotoxicity. However, when the cells were incubated with **HTN2** and irradiated with an 808-nm laser (0.8 W/cm^2), the cell viability decreased greatly because the cells were killed by the substantial heat generated by the photothermal effect of **HTN2**. These results indicated that **HTN2** has great potential for cancer therapy as an effective PTA. In addition, flow cytometry analysis was utilized to quantify the percentage of apoptosis/necrosis in the cells (Fig. 4g). Annexin V-fluorescein

isothiocyanate (FITC)$^{\pm}$-stained cells are considered to be early apoptotic cells, while PI$^{\pm}$ Annexin V-FITC^{++} staining is considered an indicator of advanced apoptosis or necrosis. The total degree of apoptosis (percentage of early and late apoptosis) in the **HTN2** + radiation group was much higher than that in the saline, saline + radiation and **HTN2** groups, indicating that the **HTN2** with radiation shows an excellent PTT effect. These data indicated that **HTN2** has potential for development as a novel organic PTA for cancer therapy.

Photothermal therapy experiments in vitro

Encouraged by the results of the experiments in vitro, we also performed related photothermal therapy experiments in vitro. To visualize the temperatures of the tumors during PTT, the temperatures of the tumor areas were recorded using an IR thermal camera. As shown in Fig. 5a, the temperatures in group 4 (**HTN2** + irradiation) increased rapidly to 65.8 °C in 2 min. In comparison, those of group 3 (saline + irradiation) remained below 43 °C. The results showed that **HTN2** had effective photothermal conversion efficiency in vivo. To further verify the tumor inhibitory effect of **HTN2** in vivo, **HTN2** was injected into tumor-bearing mice, and then an 808-nm laser (0.8 W/cm^2, 5 min) was used to activate the **HTN2**. As depicted in Fig. 5b, the tumors of the control group, including group 1 (only saline), group 2 (only **HTN2**) and group 3 (saline + irradiation), grew rapidly than group 4 (**HTN2** + irradiation), which indicated that **HTN2** had the best photothermal therapy effect. Compared with the other three groups, group 4 (**HTN2** + irradiation) exhibited favorable tumor ablation (Fig. 5c). These results showed that **HTN2** has excellent tumor inhibitory effects. Moreover, no significant differences in body weight were found in the corresponding groups (Fig. 5d), indicating that the therapeutic procedure had almost no side effects in mice. In addition, the pictures of excised tumors showed that the tumor from a mouse in group 4 (**HTN2** + irradiation) was obviously smaller than those from mice in the other three groups (Fig. 5e), further proving the great tumor inhibition effect of **HTN2**. Thereafter, the differently treated tumor tissues were separated and sliced, and histological examination was performed to further evaluate the antitumor activity of HTN2. In Fig. 5f, tumor tissue injected via saline and HTN2. The overall structure of the tumor tissue was normal, the tumor cells proliferated vigorously as black arrow shown, the tumor cells were not necrotic, and no obvious inflammatory cell infiltration was observed in the tumor tissues. As shown in Fig. 5f, the tumor tissue can be seen with necrosis only in partial area. As control group, a large number of tumor cells are necrotic, and the nucleus of the tumor cells in the necrotic area disappears, the cytoplasmic protein is degraded, and the eosin is lightly stained. leaving only a small amount of tumor cells. The organs also showed no obvious toxicity, indicating that HTN2 is safe (Fig. S14). After 12-days PTT therapy, tumor histomorphology differences between the different treated mice were significant. After the above evaluation, this indicates that treatment with HTN2 is indeed effective based on PTT. In summary, in vivo results show that HTN2-based PTT has excellent anti-tumor activity under NIR irradiation, providing a new strategy for the therapy of deep tumor tissue.

Experimental section

Reagent and instruments

1,1,2-Trimethylbenz[e]Indole, 3-Bromopropionic acid, Ethyldiisopropylamine, 3,4-Ethylenedioxythiophene, 5-Bromo-2-thiophene carboxaldehyde, 2-(7-oxidized benzotriazole)-N, N, N′, N′-tetramethylurea hexafluorophosphate and Palladium(II) acetate were purchased from Energy Chemical (Shanghai, China), butyllithium, N-bromosuccinimide, 4-ethenyl-N, N-dimethylaniline, tetrabutylammonium bromide were obtained from Macklin Biochemical Co. Ltd (Shanghai, China). 3-(4, 5-Dimethylthialzol-2-yl)-2, 5-diphe-nyltetrazolium bromide (MTT), Dulbecco's modified Eagle medium (DMEM), fetal bovine serum (FBS), penicillin, and streptomycin were obtained from Alfa Aesar Chemical Company. All other solvents and reagents used in the experiment are certified analytical reagent grades.

Nuclear magnetic resonance (NMR) spectra were detected by Bruker Advance III-300 instrument (Bruker, Billerica, MA, USA) at 400 MHz and 600 MHz for 1H NMR and 13C NMR, in which tetramethylsilane (TMS) was utilized as an internal standard (0 ppm). Mass spectra were obtained by tandem quadrupole mass spectrometer (Waters, Milford, MA, USA) with ESI resource and AB SCIEX 5800 matrix-assisted laser desorption ionization time-of-flight (MALDI-TOF) mass spectrometer (SCIEX, Beijing, China) respectively. Absorption spectra were recorded on Hitachi U-3310 spectrophotometer (Hitachi Tokyo, Japan), and fluorescence spectra were measured by Agilent Cary Eclipse fluorophotometer (Varian, USA). All confocal fluorescence images were obtained from Zeiss LCSM 700 microscope laser confocal scanning microscopy (LCSM). TES-1320 Dual Digital Thermometer Temperature Reader (Jingchuang Electronics Manufacturing Co., Ltd). Flow cytometry (Thermo Fisher Scientific Inc). IR thermal camera (FLIR® Systems, Inc).

Synthesis and characterization of HTN1-4

We conjugated the thiophene derivatives and indole salt derivatives to design novel molecules with NIR fluorescence molecules and absorption at long wavelengths. The synthetic route of HTN1-4 is shown in Fig. 1a and the details of the steps to prepare **HTN1, 3,** and **4** are shown in Fig. S1. We confirmed the structures of **HTN1-4** based on their ^{1}H NMR spectra, ^{13}C NMR spectra, and MS spectra (Fig. S2).

HTN2: The mixture of D-Glucosamine hydrochloride (32.8 mg, 0.15 mmol), 2-(7-oxidized benzotriazole)-N, N, N′, N′-tetramethylurea hexafluorophosphate (HATU) (57.75 mg, 0.15 mmol), DIEA (23.31 μL, 0.075 mmol) in anhydrous DMF (1 mL) were stirred at 0 °C for 10 min in the dark in nitrogen protected environment. Then the solution of compound HTN1 (50 mg, 0.075 mmol) and ethyl diisopropylamine (23.31 μL, 0.075 mmol) were added dropwise at 0 °C overnight. The reaction was monitored by thin-layer chromatography (TLC). The solvent was removed under reduced pressure after the reaction. The crude product was purified by the silica gel column chromatography with DCM/Methanol (3:1) as the eluent. Then the product was recrystallized by diethyl ether and DCM to acquire blue powder (15 mg, 24.2% yield). ^{1}H NMR (400 MHz, Methanol d_4) δ (ppm): 8.52 (s, 1H), 8.32 (d, J = 8.8 Hz, 2H), 8.18 (d, J = 8.5 Hz, 1H), 8.11 (d, J = 8.3 Hz, 1H), 8.07 (d, J = 8.0 Hz, 1H), 7.84–7.78 (m, 1H), 7.72 (t, J = 7.7 Hz, 1H), 7.60 (t, J = 7.5 Hz, 1H), 7.46–7.40 (m, 2H, Ar-H), 7.31 (s, 1H), 7.27 (d, J = 4.2 Hz, 1H), 7.09 (dd, J = 16.0, 5.3 Hz, 1H), 6.70 (d, J = 8.3 Hz, 2H, Ar-H), 4.73 (s, 3H), 4.59 (s, 4H), 4.46 (s, 2H), 3.85 (d, J = 4.0 Hz, 1H), 3.72 (dd, J = 7.8, 6.0 Hz, 3H), 3.65 (dd, J = 6.9, 4.7 Hz, 3H), 3.05 (dd, J = 7.4, 1.6 Hz, 2H), 3.00 (s, 6H), 2.02 (s, 6H). ^{13}C NMR (151 MHz, Methanol d_4) δ (ppm): 180.54, 171.97, 152.85, 148.86, 140.15, 136.25, 134.32, 132.12, 131.18, 130.23, 129.18, 128.70, 127.47, 124.99, 123.78, 121.15, 113.22, 113.06, 92.51, 90.82 , 74.30, 73.00, 72.37, 71.31, 67.78, 66.91, 66.07, 64.31, 62.61, 56.23, 56.01, 55.71, 53.92, 40.28, 36.57, 27.47, 15.45. MALDI-TOF-MS: m/z = 740.78, calculated exact mass = 740.34

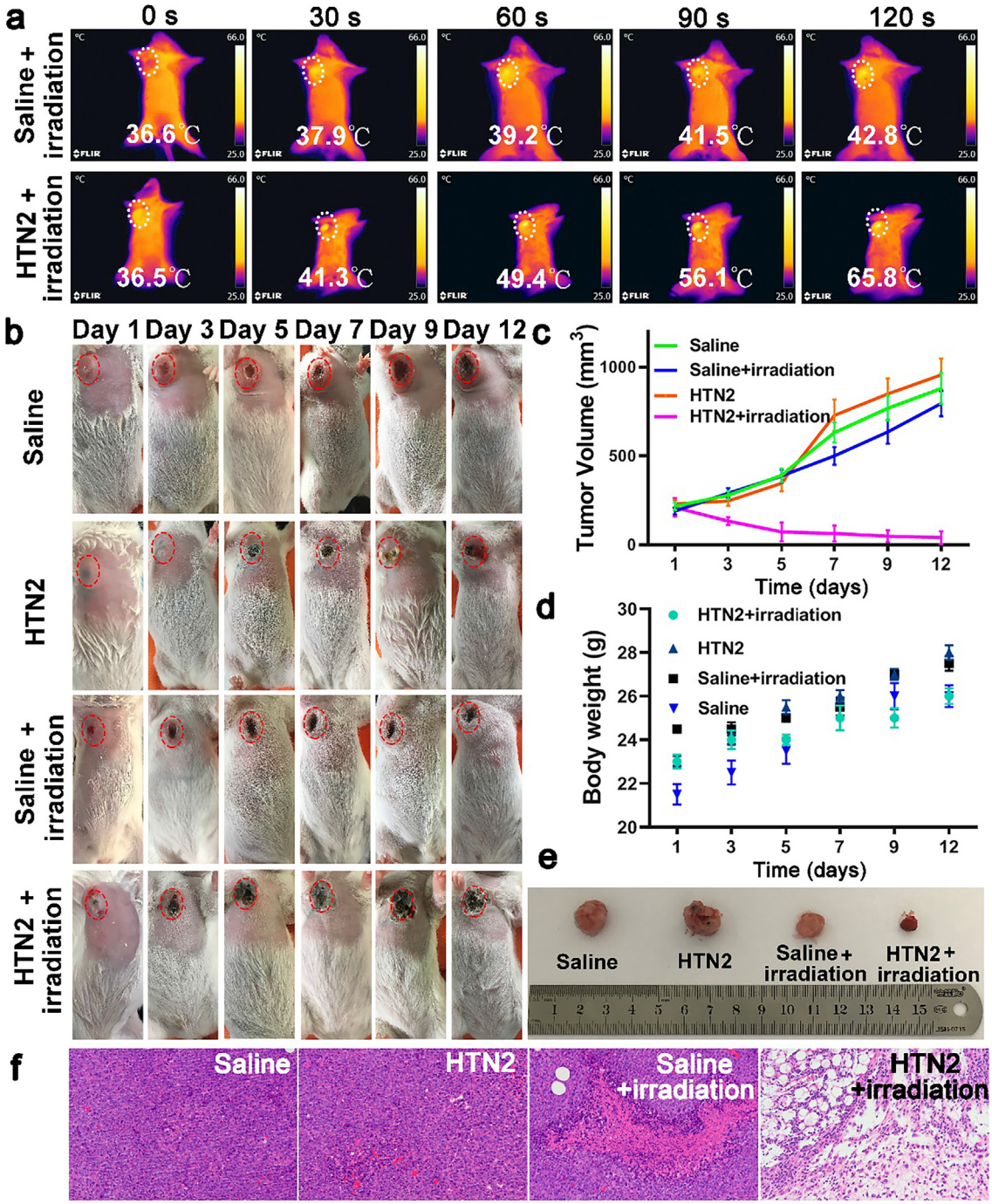

Fig. 5. PTT efficiency in EAC tumor-bearing mice after treatment with **HTN2** and an 808-nm laser. (a) Photographs of the mice during 808-nm laser irradiation (0.8 W/cm^2) at different time points. (b) Photographs of mice in different groups on day 1, day 3, day 5, day 7, day 9 and day 12 after photothermal treatment. (c) The tumor volumes in different mice groups (mean ± SD, n = 5). (d) The weight of mice in different groups over time (mean ± SD, n = 5). (e) Pictures of representative excised tumors from different groups on the 12th day. Histomorphological examination. H&E-stained tissue sections, in which saline-injected tumor tissue and mouse tumor tissue were injected with HTN2 for PTT treatment tumor mice were injected with saline and irradiated PTT Treated control group with HTN2 and irradiated, which were harvested from tumor mice after 12-days treatment.

DFT calculations

The photoelectric performance of **HTN1-4** was evaluated by time-dependent density functional theory (TD-DFT) with B3LYP functional analysis at the 6-31G* level of theory. Calculations were accomplished with the commercial Gaussian 09 software package. Molecular orbitals were illustrated using the Gabedit 2.4.8 software package.

Detection of in vitro optical properties

All UV–Vis spectra were measured in phosphate buffered saline (PBS) containing 1% DMSO at pH 7.4, and the fluorescence spectra were acquired in PBS containing 10% DMSO because of its weak fluorescence in the aqueous phase. Absorption spectra were recorded in the range from 400 nm to 1100 nm and fluorescence spectra were collected in the range from 700 to 900 nm with λ_{ex} = 650 nm.

The photothermal effect and photothermal stability of HTN1-4

First, the appropriate amounts of **HTN1-4** based on their different molecular weights were accurately weighed and completely dissolved in DMSO to prepare solutions with final concentrations of 0 mM, 0.25 mM, 0.5 mM, and 1 mM. A 100 μL aliquot of each homogenous solution was added to a 96-well plate to prepare the photothermal effect curves at different concentrations and different powers of the 635-nm and 808-nm laser (0, 0.4, 0.8, and 1.2 W/cm^2). The solution was probed with a needle thermometer. The changes in temperature during 600 s of laser irradiation were plotted. To evaluate the photothermal stability of **HTN1-4**, repeated irradiation and cooling cycles were performed in DMSO at a power 0.8 W/cm^2 with 635-nm and 808-nm laser. The temperature profile during passive cooling to room temperature was recorded by a needle thermometer within the 900 s of the irradiation/cooling cycle. Control compound **HTN** was tested as same condition with 532-nm laser.

Cell culture

The cell lines involved in this experiment were all from the American Type Culture Collection (ATCC), and the human glioma cell line U87 was used. The above cell line was maintained in DMEM supplemented with 10% (v/v) fetal bovine serum and both penicillin (10,000 U/mL) and streptomycin (10,000 g/mL) (100×) at 37 °C in a 5% CO_2 incubator. The trypsin-EDTA solution used in this study contained 0.25% trypsin and 0.02% EDTA.

Cytotoxicity assay

To verify the biocompatibility of the two probe molecules at the cellular level, cell viabilities were measured by MTT colorimetry. MTT (0.5 g) was dissolved in 100 mL of PBS or phenol red-free medium. The bacteria in the solution were removed by filtration through a 0.22-μm filter, and for these studies, the U87 cell line was used as target cells. The cells were cultured in a cell culture dish to the logarithmic growth phase, trypsinized, pipetted, and centrifuged at 1200 rpm. A cell suspension was then prepared using DMEM containing 10% fetal bovine serum, and the cells were transferred to a 96-well plate. The density was 2×10^5 cells per well, and the cells were cultured overnight at 37 °C in a 5% CO_2 incubator to form a monolayer. The two probes were first dissolved in DMSO to final concentrations of 10 mM to afford stock solutions, and these stock solutions were diluted in batches with DMEM containing 10% fetal bovine serum to 5 μM, 10 μM, 20 μM, 40 μM, 60 μM and 80 μM. The solutions at these six concentrations were cultured in a 96-well plate at 100 μL per well for 12 h. After the completion of the culture, the medium in the wells of the 96-well plate was aspirated, and the cells were washed three times with sterile PBS (pH = 7.4). MTT medium at 5 mg/mL was added to each well, and the cells were incubated for an additional 4 h, and after this, the remaining solution was aspirated. Sterile DMSO (100 μL) was added to each well of the well plate, and the plate was placed in a horizontal shaker and shaken for 20 min to fully dissolve the blue-purple formazan crystals. The OD value at 560 nm in the 96-well plate was measured with a microplate reader. Six replicate wells were used for each group. The cell viability was calculated based on the following equation: cell viability (%) = (average absorbance of the administration group / average absorbance of the control group) × 100%.

Penetration ability of HTN2 in Three-dimensional U87 tumor sphere

To further explore the ability of **HTN2** to penetrate tumors at the cellular level, we used agarose with a low pH, low oxygen and high internal pressure, similar to the tumor microenvironment to prepare a three-dimensional tumor sphere model. One milliliter aliquot of 2% low-melting agarose that had been heated and melted were transferred to a 6-well plate. After the agarose cooled and solidified, we seeded U87 cells (1×10^5 ml^{-1}) in each well and incubated for 4 days. The solution of **HTN2** was added dropwise to a six-well plate and incubation continued for two hours. Finally, the spheroids were pipetted in a confocal culture dish with a pipette, and the fluorescence intensity in the three-dimensional U87 tumor sphere was observed under a laser scanning confocal microscope (LSCM), and the Z-stack map of the tumor sphere was analyzed.

Subcellular localization and bioimaging of cell uptake

The subcellular localization of **HTN2** was determined by co-staining with Droplit™ Red (ATT Bioquest, America). The whole staining procedure was carried out at 37 °C in the dark. Finally, fluorescent images were acquired by LCSM and processed using ZEN imaging software. Fluorescence signals of different commercial localization probes and **HTN2** were collected in the various fluorescent channels that were recommended by the manufacturer. To verify the cellular uptake kinetics of **HTN2**, U87 cells were incubated with 20 μM **HTN2** for different times (0.5 h, 1 h, and 2 h). Semiquantitative analysis of the relative fluorescence intensity of each group was carried out to determine the uptake kinetics of the cells for the different probes.

IR thermal imaging

Cells treated with saline or **HTN2** were irradiated with an 808-nm laser at a power density of 0.8 W/cm^2 for 2 min. To monitor the temperature of the tumor during PTT, the temperature was recorded with an IR thermal camera. ICR-SPF mice (6–8 weeks old, female, 20–25 g) were purchased from Qinglongshan Animal Center (Nanjing, China) for the in vivo therapy investigation. All animal experiments were carried out in compliance with the Animal Management Rules of the Ministry of Health of People's Republic of China (document no. 55, 2001) and the Guidelines for the Care and Use of Laboratory Animals of China Pharmaceutical University. To establish the tumor xenograft models, 2×10^6 EAC (Ehrlich ascites carcinoma) cells in 200 μL of solution were injected subcutaneously into the right flank of each mouse to obtain the EAC tumor-bearing mouse model. When the tumor volume reached approximately 200 mm^3, 20 μL of **HTN2** solution (1 mM, DMSO: PBS = 1:9, v: v) was intratumorally administered into the EAC tumor-bearing mice. The control group was injected with saline. Then, the tumor areas were irradiated with an 808 nm laser (0.8 W/cm^2, 2 min) with simultaneously monitoring with an IR thermal camera (FLIR® Systems, Inc.). The temperatures of the tumor areas were recorded at different times (0 s, 30 s, 60 s, 90 s, and 120 s).

Photothermal ablation of cancer cells

To explore the actual antitumor effect of **HTN2** in vitro, the cells in the LSCM culture dish were transferred to a well plate at a density of 2×10^5 cells per well and then incubated at 37 °C and 5% CO_2 in an air. Once the cells reached the log phase, they were then treated with **HTN2** (20 μM) in DMSO-PBS (1:99, v: v) for 15 min. Subsequently, each cell culture dish was irradiated with 808-nm laser at different laser powers (0 W/cm^2, 0.4 W/cm^2, and 0.8 W/cm^2) for 2 min. Confocal fluorescence images of the U87 cells were acquired after incubation for 2 h with 20 μM **HTN2** and 5 μM propidium iodide (PI) (DEAD Cell Imaging Kit) under different 808-nm laser powers (0 W/cm^2, 0.4 W/cm^2 and 0.8 W/cm^2).

The photothermal experiment was performed in a 96-well plate using the MTT method. The effects of different concentrations (0 μM, 5 μM, 10 μM, 20 μM, 40 μM, 60 μM, and 80 μM) of the test compound for the photothermal treatment of the human glioma cell line U87 were explored. First, U87 cells were incubated overnight in 96-well plates to form a monolayer. Then, the probe molecules at six different concentrations were added, and after incubation with the U87 cells for 12 h, the medium was aspirated, and the cells were washed three times with sterile PBS. DMEM containing 10% fetal calf serum was added to each well. Finally, the U87 cells were irradiated with an 808-nm laser for 10 min at a power density of 0.8 W/cm^2 and then cultured for an additional 4 h. After aspiration of the medium, the cells were washed three times with sterile PBS, MTT at a concentration of 5 mg/mL was added to each well, and the cells were incubated for an additional 4 h. After the incubation, the medium in each well of the 96-well plate was carefully aspirated, 100 μL of sterile DMSO was added to each well, and the plate placed in a horizontal shaker and shaken for 20 min to completely dissolve the formazan crystals. The wells were then assessed using a microplate reader. The OD_{560} values were measured, and 6 replicate wells were used per group. The photothermal antitumor effects were calculated in accordance with the method for calculating cell viability in the cytotoxicity test described above.

Flow cytometry analysis

Flow cytometry analysis of apoptosis was performed to further verify the antitumor effect of the photothermal therapy. U87 cells were cultured overnight in four cell culture dishes at 37 °C in 5% CO_2. Once the cells formed a single cell layer, PBS, 20 μM and 40 μM probe solution were added to the cell culture dishes, and the cells were incubated for 2 h. The medium was removed and replaced with fresh fetal bovine serum after this incubation. Then, the saline and **HTN2** groups were irradiated with an 808-nm laser at a power of 0.4 W/cm^2 for 2 min, and the two unirradiated groups were set as the control groups. The cells were collected by trypsinization without EDTA and washed twice with saline (2000 rpm, centrifugation for 2 min) to collect 1–5 × 10^5 cells in tubes. The cells were co-stained with Annexin V-FITC (5 μL) and propidium iodide (5 μL). The reaction was conducted with protection from light for 5–15 min at room temperature, and flow cytometry was used to measure apoptosis. Among the tested probes, the green fluorescence of Annexin V-FITC was detected by the FL1 channel with an excitation wavelength of 488 nm and emission wavelength of 530 nm. The red fluorescence of PI was detected with the FL2 channel with an excitation wavelength of 488 nm and an emission wavelength of 630 nm. Fluorescence compensation adjustment was performed to remove spectral overlap and determine the position of the intersection.

Tumor ablation induced by photothermal effects

The tumor inhibition by **HTN2** via photothermal effect was further investigated. Twenty EAC-tumor-bearing mice were randomly divided into four groups when their tumor volume reached approximately 200 mm^3. The mice in group 1 were intratumorally injected with saline solution; the mice in group 2 were intratumorally injected with 40 μL of **HTN2** solution (1 mM, DMSO: PBS = 1:9, v:v); the mice in group 3 were intratumorally injected with saline solution and exposed to a 808-nm laser (0.8 W/cm^2, 2 min); and the mice in group 4 were intratumorally injected with 40 μL of **HTN2** solution (1 mM, DMSO:PBS = 1:9, v:v) and exposed to an 808-nm laser (0.8 W/cm^2, 2 min) every other day. The weight and tumor sizes of the mice were measured using an electronic balance and a Vernier caliper after PTT treatment. The tumor volume (V) was calculated based on the formula: V = a * b^2/2 (a: length of tumor, b: width of tumor).

Conclusions

In summary, we developed a series of PTAs based on a D-π-A system for enhancing PTT effect, and HTN1-4 showed different absorption wavelengths, fluorescence characteristics, and photothermal properties. After extensive experiments and careful theoretical calculations, we found that **HTN2** possesses the greatest potential as PTA for cancer therapeutic. According to further biological experiments, **HTN2** had the best photothermal effect and good cytotoxicity, and most cancer cells can be ablated by the photothermal effect of **HTN2**. Notably, **HTN2** also shows excellent LDs targeting. Relatively low irradiation times and intensities were utilized to achieve the best therapeutic effect and biosafety in targeting the LDs. Therefore, this study found that **HTN2** can be used as an LDs-mediated PTA and achieve an enhanced PTT synergistic effect during cancer therapy processes.

Declaration of Competing Interest

The authors declare that they have no known competing financial interests or personal relationships that could have appeared to influence the work reported in this paper.

Acknowledgments

We are grateful to the Natural Science Foundation Committee of China (NSFC 81671803), the Post-doctoral Innovative Talent Support Program (BX20190389), the Outstanding Youth Foundation of Jiangsu Province (GX20171114003, BK20170030), China Postdoctoral science Foundation (2019M662009), "Double First-Class" University project (CPU2018GY06) and Postdoctoral Research Grant of Jiangsu Province.

Appendix A. Supplementary material

Supplementary data to this article can be found online at https://doi.org/10.1016/j.jare.2020.08.003.

References

[1] Liu Y, Bhattarai P, Dai Z, Chen X. Photothermal therapy and photoacoustic imaging via nanotheranostics in fighting cancer. Chem Soc Rev 2019;48(7):2053–108.
[2] Huang X, Zhang W, Guan G, Song G, Zou R, Hu J. Design and Functionalization of the NIR-Responsive Photothermal Semiconductor Nanomaterials for Cancer Theranostics. Acc Chem Res 2017;50(10):2529–38.
[3] Lee MH, Sharma A, Chang MJ, Lee J, Son S, Sessler JL, et al. Fluorogenic reaction-based prodrug conjugates as targeted cancer theranostics. Chem Soc Rev 2018;47(1):28–52.
[4] Du Y, Ding Y, Ge F, Wang X, Ma S, Lu H, et al. A regular ternary conjugated polymer bearing π-extended diketopyrrole and isoindigo acceptor units for field-effect transistors and photothermal conversion. Dyes Pigm 2019;164:27–34.
[5] Pang J, Tao L, Lu X, Yang Q, Pachauri V, Wang Z, et al. Photothermal effects induced by surface plasmon resonance at graphene/gold nanointerfaces: A multiscale modeling study. Biosens Bioelectron 2019;126:470–7.
[6] Wang Z, Yu N, Li X, Yu W, Han S, Ren X, et al. Galvanic exchange-induced growth of Au nanocrystals on CuS nanoplates for imaging guided photothermal ablation of tumors. Chem Eng J 2020;381:122613.
[7] Li Q-L, Sun Y, Ren L, Wang X, Wang C, Li L, et al. Supramolecular Nanosystem Based on Pillararene-Capped CuS Nanoparticles for Targeted Chemo-Photothermal Therapy. ACS Appl Mater Interfaces 2018;10(35):29314–24.
[8] Shi H, Sun Y, Yan R, Liu S, Zhu L, Liu S, et al. Magnetic Semiconductor Gd-Doping CuS Nanoparticles as Activatable Nanoprobes for Bimodal Imaging and Targeted Photothermal Therapy of Gastric Tumors. Nano Lett 2019;19(2):937–47.
[9] Zhang Y, Song N, Li Y, Yang Z, Chen L, Sun T, et al. Comparative study of two near-infrared coumarin-BODIPY dyes for bioimaging and photothermal therapy of cancer. J Mater Chem B 2019;7(30):4717–24.

[10] Meng Y, Wang S, Li C, Qian M, Yan X, Yao S, et al. Photothermal combined gene therapy achieved by polyethyleneimine-grafted oxidized mesoporous carbon nanospheres. Biomaterials 2016;100:134–42.
[11] Zhang M, Zheng T, Sheng B, Wu F, Zhang Q, Wang W, et al. Mn2+ complex-modified polydopamine- and dual emissive carbon dots based nanoparticles for in vitro and in vivo trimodality fluorescent, photothermal, and magnetic resonance imaging. Chem Eng J 2019;373:1054–63.
[12] Sun S, Chen J, Jiang K, Tang Z, Wang Y, Li Z, et al. Ce6-Modified Carbon Dots for Multimodal-Imaging-Guided and Single-NIR-Laser-Triggered Photothermal/Photodynamic Synergistic Cancer Therapy by Reduced Irradiation Power. ACS Appl Mater Interfaces 2019;11(6):5791–803.
[13] Chen L, Zhang Y, Song N, Li Y, Xie Z. Comparison Study of Two Near-Infrared Coumarin-BODIPY Dyes for Bioimaging and Photothermal Therapy of Cancer. J Mater Chem B 2019;7(30).
[14] Zhang D, Du S, Su S, Wang Y, Zhang H. Rapid detection method and portable device based on the photothermal effect of gold nanoparticles. Biosens Bioelectron 2019;123:19–24.
[15] Feng Z, Yu X, Jiang M, Zhu L, Zhang Y, Yang W, et al. Excretable IR-820 for in vivo NIR-II fluorescence cerebrovascular imaging and photothermal therapy of subcutaneous tumor. Theranostics 2019;9(19):5706–19.
[16] Chen X, Lee D, Yu S, Kim G, Lee S, Cho Y, et al. In vivo near-infrared imaging and phototherapy of tumors using a cathepsin B-activated fluorescent probe. Biomaterials 2017;122:130–40.
[17] Lu S, Lei X, Ren H, Zheng S, Qiang J, Zhang Z, et al. PEGylated Dimeric BODIPY Photosensitizer as Nanocarrier for Combined Chemotherapy and Cathepsin B-activated Photodynamic Therapy in 3D Tumor Spheroids. ACS Appl Bio Mater 2020.
[18] Wang H, Chang J, Shi M, Pan W, Li N, Tang B. A Dual-Targeted Organic Photothermal Agent for Enhanced Photothermal Therapy. Angew Chem Int Ed 2019;58(4):1057–61.
[19] Pan G-Y, Jia H-R, Zhu Y-X, Wang R-H, Wu F-G, Chen Z. Dual Channel Activatable Cyanine Dye for Mitochondrial Imaging and Mitochondria-Targeted Cancer Theranostics. ACS Biomater Sci Eng 2017;3(12):3596–606.
[20] Cao J, Chi J, Xia J, Zhang Y, Han S, Sun Y. Iodinated Cyanine Dyes for Fast Near-Infrared-Guided Deep Tissue Synergistic Phototherapy. ACS Appl Mater Interfaces 2019;11(29):25720–9.
[21] Yan Y, Chen J, Yang Z, Zhang X, Liu Z, Hua J. NIR organic dyes based on phenazine-cyanine for photoacoustic imaging-guided photothermal therapy. J Mater Chem B 2018;6(45):7420–6.
[22] Wang Z, Gai S, Wang C, Yang G, Zhong C, Dai Y, et al. Self-assembled zinc phthalocyanine nanoparticles as excellent photothermal/photodynamic synergistic agent for antitumor treatment. Chem Eng J 2019;361:117–28.
[23] Jiang B-P, Hu L-F, Shen X-C, Ji S-C, Shi Z, Liu C-J, et al. One-Step Preparation of a Water-Soluble Carbon Nanohorn/Phthalocyanine Hybrid for Dual-Modality Photothermal and Photodynamic Therapy. ACS Appl Mater Interfaces 2014;6(20):18008–17.
[24] Gao DY, Zhang BY, Liu YB, Hu DH, Sheng ZH, Zhang XJ, et al. Molecular Engineering of Near-Infrared Light-Responsive BODIPY-Based Nanoparticles with Enhanced Photothermal and Photoacoustic Efficiencies for Cancer Theranostics. Theranostics 2019;9(18):5315–31.
[25] Liu Y, Song N, Chen L, Liu S, Xie Z. Synthesis of a Near-Infrared BODIPY Dye for Bioimaging and Photothermal Therapy. Chemistry – An Asian Journal 2018;13(8):989–95.
[26] Zhang W, Lin W, Li C, Liu S, Hu X, Xie Z. Rational Design of BODIPY-Diketopyrrolopyrrole Conjugated Polymers for Photothermal Tumor Ablation. ACS Appl Mater Interfaces 2019;11(36):32720–8.
[27] Babu DD, Gachumale SR, Anandan S, Adhikari AV. New D-π-A type indole based chromogens for DSSC: Design, synthesis and performance studies. Dyes Pigm 2015;112:183–91.
[28] Liu W, Li B, Gao H, Wang D, Wang L, Yang Z, et al. NIR absorbing thiophene derivatives with photoacoustic and photothermal effect used in drug release. Dyes Pigm 2019;162:331–8.
[29] Tirinato L, Liberale C, Di Franco S, Candeloro P, Benfante A, La Rocca R, et al. Lipid droplets: a new player in colorectal cancer stem cells unveiled by spectroscopic imaging. Stem cells 2015;33(1):35–44.
[30] Abramczyk H, Surmacki J, Kopeć M, Olejnik AK, Lubecka-Pietruszewska K, Fabianowska-Majewska K. The role of lipid droplets and adipocytes in cancer. Raman imaging of cell cultures: MCF10A, MCF7, and MDA-MB-231 compared to adipocytes in cancerous human breast tissue. Analyst 2015;140(7):2224–35.
[31] Bozza PT, Viola JP. Lipid droplets in inflammation and cancer, Prostaglandins. Leukotrienes and Essential Fatty Acids (PLEFA) 2010;82(4–6):243–50.
[32] Frank R, Najbauer J, Aboody K. Concise Review: Stem Cells As an Emerging Platform for Antibody Therapy of Cancer. Stem cells (Dayton, Ohio) 2010;28:2084–7.
[33] Chen S-Y, Huang Y-C, Liu S-P, Tsai F-J, Shyu W, Lin S-Z. An Overview of Concepts for Cancer Stem Cells. Cell Transplant 2010;20:113–20.
[34] Jung HS, Verwilst P, Sharma A, Shin J, Sessler J, Kim J. Organic molecule-based photothermal agents: An expanding photothermal therapy universe. Chem Soc Rev 2018;47:2280–97.
[35] Li L, Xu Y, Chen Y, Zheng J, Zhang J, Li R, et al. A family of push-pull bio-probes for tracking lipid droplets in living cells with the detection of heterogeneity and polarity. Anal Chim Acta 2020;1096:166–73.
[36] Ren W, Yan Y, Zeng L, Zhenzhi S, Gong A, Schaaf P, et al. A Near Infrared Light Triggered Hydrogenated Black TiO2 for Cancer Photothermal Therapy. Adv Healthcare Mater 2015;4.
[37] Liu Y, Ai K, Jianhua L, Deng M, He Y, Lu L. Dopamine-Melanin Colloidal Nanospheres: An Efficient Near-Infrared Photothermal Therapeutic Agent for In Vivo Cancer Therapy, Advanced materials (Deerfield Beach. Fla.) 2013;25.
[38] Liu Q, Luo Q, Halim A, Song G. Targeting lipid metabolism of cancer cells: A promising therapeutic strategy for cancer. Cancer Lett 2017;401:39–45.
[39] Perez-Hernandez M, del Pino P, Mitchell S, Moros M, Stepien G, Pelaz B, et al. Dissecting the Molecular Mechanism of Apoptosis during Photothermal Therapy Using Gold Nanoprisms. ACS Nano 2014;9.
[40] Abadeer NS, Murphy CJ. Recent Progress in Cancer Thermal Therapy Using Gold Nanoparticles. J Phys Chem C 2016;120(9):4691–716.